Malaysian Journal of Chemistry, 2025, Vol. 27(2), 10-21

Comparison Study of Pt Decorated Bi_2WO_6/g-C_3N_4 by Batchwise and One-step Preparation Techniques for the Photodegradation of RR4 Dye

Nur Syamimi Adzis, Qoid Syauqi Syahid, Rahil Azhar, Nur Izzati Nabilah Zainal,
Nur Hidayatul Syazwani Suhaimi, Mohd Azlan Mohd Ishak and Wan Izhan Nawawi*
Faculty of Applied Sciences, Universiti Teknologi MARA (UiTM), 02600 Arau, Perlis, Malaysia
*Corresponding author (e-mail: wi_nawawi@uitm.edu.my)

A Z-Scheme heterojunction comprising photocatalysts Bi_2WO_6 and g-C_3N_4 doped with platinum was successfully synthesized by two distinctive methods, batchwise & one-step, to degrade a model pollutant, RR4 dye. Several instruments including FTIR, XRD, UV-VIS, photoluminescence (PL analysis), FESEM-EDX and photoelectrochemistry were used to characterize the sample obtained. FTIR spectra depicted intense sharp peaks at 810 cm^{-1} which were assigned to s-triazine units of CN. The C-N stretching vibration mode was also detected in the region of 1200–1750 cm^{-1}. The crystallite sizes of the prepared photocatalysts were determined by XRD diffraction, where the Scherrer equation was applied to calculate the size. In XRD, the diffraction angles of Bi2WO6 were exhibited at 28.6°, 33.1, 47.4°, 56.2°, 59.1°, 69.2° and 78.8°, and these angles were also seen in a variety of composites. From UV-Vis analysis, pristine Bi_2WO_6 had an absorption edge of approximately 443 nm, which corresponded to a band gap of approximately 2.6 eV. The absorption edge of pure g-C_3N_4 was at about 457 nm, corresponding to a band gap of 2.8 eV. Upon fabrication of the Z-scheme heterojunction, no band gap reduction occurred. All modified and unmodified Bi_2WO_6/g-C_3N_4 samples showed photocatalytic degradation efficiencies of up to 50 %, and the composites prepared by one-step and batchwise techniques (hereinafter referred to as PBCN (OS) and PBCN (B) respectively) achieved 80 % photodegradation of RR4 dye.

Keywords: Photocatalysis; Z-scheme heterojunction; dye degradation; platinum; electron mediator

Received: July 2024; Accepted: November 2024

Every year, water pollution from the industrial sector escalates and gets out of hand. The textile processing industry produces substantial amounts of wastewater because the dyeing, finishing, and washing stages require an enormous amount of water and release undesirable effluents into water bodies [1]. These effluents not only carry a variety of toxic recalcitrant dyes and dissolved solids, but also contain organic compounds that are harmful to the environment. Once released, these pollutants remain in the environment for an extended period [2]. Advanced Oxidation Processes (AOPs) are considered promising techniques for eliminating emerging pollutants such as dyes from wastewater discharges. Photocatalysis is one AOP technique that has become a research hotspot in wastewater treatment as it effectively degrades and mineralizes dyes in wastewater, compared to current conventional methods such as chemical treatment using alum which is expensive and less effective for organic pollutants [3]. However, synthesis of the ideal photocatalyst remains the biggest challenge.

Among various photocatalysts, Bi_2WO_6 is proficient as an active visible-light photocatalyst for organic contaminant degradation [4]. Owing to its narrow bandgap at 2.8 eV and non-toxic nature, Bi_2WO_6 has been used for the degradation of micropollutants [5]. However, Bi_2WO_6 suffers from rapid electron-hole (e^-/h^+) recombination where the charge carriers tend to recombine due to the low band gap energy that may lead to low photocatalytic activity [6]. Thus, researchers have proposed several modifications including metal deposition [7], nonmetal doping [8], morphological modifications [9] and construction of heterojunctions by coupling with another semiconductor [10]. Among these modifications, coupling with another semiconductor to produce a heterojunction system was chosen as it promotes light absorption properties, improves chemical stability, and enhances photoexcited charge separation, thus effectively boosting photocatalysis [11]. Among all semiconductors, graphitic carbon nitride (g-C_3N_4) is one organic semiconductor that has caught the attention of researchers because of its outstanding stability in stacking structures, non-toxic properties and high absorption capability [7, 12]. g-C_3N_4 has a wide band gap energy at around 2.7-2.8 eV due to a high recombination rate and weak charge separation process. Hence, the combination of g-C_3N_4 with Bi_2WO_6 may improve the overall charge transfer efficiency through the heterojunction effect [13, 14].

Recent studies have reported several mechanisms for heterojunctions, including the Schottky junction, Type II, direct Z-schemes, and p-n junction. Among all, the Z-scheme appears to be the best and most reliable method as it promotes better light absorption capacity and potentially overcomes the drawback of rapid charge carrier recombination [15]. However, a heterojunction of these materials has a high tendency to become a type-II heterojunction which gives unsatisfactory results. Therefore, doping a noble metal to function as an electron mediator is a viable alternative to construct a stable Z-Scheme heterojunction [16]. However, fabrication of a Z-scheme heterojunction through the batchwise preparation method leads to low photocatalytic activity [17]. Previous studies have claimed that inserting Pt as an effective electron mediator into a Z-Scheme heterojunction by a one-step preparation could improve photocatalytic performance [18]. Thus, this study was conducted to justify this claim by the fabrication of Z-Scheme heterojunctions prepared by two distinctive methods, batchwise & one-step. These were then compared to identify which preparation method could significantly boost photocatalytic activity, using Reactive Red 4 (RR4) dye as a model pollutant.

EXPERIMENTAL

Chemicals and Materials

The photodeposition of Pt onto Bi_2WO_6 was prepared according to a one-step preparation method. Chemicals used in this experiment were bismuth (III) nitrate pentahydrate ($Bi(NO_3)_3.5H_2O$) and sodium tungstate dihydrate ($Na_2WO_4.2H_2O$), which were supplied by Merck. Chloroplatinic acid (H_2PtCl_6) was used as a platinum precursor, sodium borohydride ($NaBH_4$) as a strong reducing agent, urea as a carbon nitride precursor, and RR4 dye as the model pollutant.

Other equipment used included a glass cell (15 x 20 x 0.5 cm), 250 mL Schlenk tube, cellulose acetate (CA) syringe filter, 10 mL syringe, a 55 Watt fluorescent lamp model Firefly/E27 as the light source, a hydrothermal reactor, and a 20 mL Teflon vessel.

One-step Preparation

Bi_2WO_6 was prepared by separately mixing 0.44 g of sodium tungstate dihydrate ($Na_2WO_4.H_2O$) and 1.29 g bismuth (III) nitrate pentahydrate ($Bi(NO_3)_3.5H_2O$) in 7.5 mL of deionized water (DI water) until both turned into colourless solutions. Then, the prepared $Na_2WO_4.2H_2O$ solution was added dropwise to the $Bi(NO_3)_3.5H_2O$ solution and vigorously stirred for 2 hours at room temperature until fully dissolved. Approximately 0.28 mL of a reducing agent, $NaBH_4$. was mixed with 0.5, 1.0, 1.5 and 2.0 % solutions of chloroplatinic acid (H_2PtCl_6) respectively. Next, the mixture was transferred into a Teflon vessel and heated up to 180 °C for 24 hours, with a heating rate of 5 °C/min. The product collected after centrifugation at 4000 rpm for 30 minutes was washed with DI water and ethanol a few times to remove any impurities. The sample was left to dry overnight in the oven at 80 °C.

Batchwise Preparation

Bi_2WO_6 was prepared in a manner similar to the one-step preparation, in which the precursors used were $Na_2WO_4.2H_2O$ and $Bi(NO_3)_3.5H_2O$ solutions. After combining the precursors, the mixture was transferred into a Teflon vessel and heated for 24 hours at 180 °C. The product obtained (Bi_2WO_6) was cooled to room temperature and dried in the oven for 8 hours at 80 °C. Next, the photocatalyst obtained was ground. The prepared Bi_2WO_6 was coupled with g-C_3N_4 via calcination before doping. To platinize the Bi_2WO_6, about 0.5 gram of the prepared Bi_2WO_6/g-C_3N_4 composite was mixed with 0.5, 1.0, 1.5 and 2.0 % of H_2PtCl_6, respectively, in 10 ml of isopropanol/water solution in a Schlenk tube. The formulation was purged with nitrogen gas under vacuum to prevent the oxidation of platinum. For 1 hour, the mixture was photo-deposited under 250 Watt consistent light irradiation. Lastly, the samples were centrifuged and dried at 80 °C for 8 hours.

Photocatalytic Degradation of RR4 Dye

The photocatalytic activity of Pt-Bi_2WO_6/g-C_3N_4 was evaluated by its degradation of RR4 dye. A 20 ml sample of 10 ppm RR4 dye in suspension form was irradiated with a 55 W fluorescent lamp model Firefly/E27 (UV: 6.9, VIS 461) for 15 minutes until the dye solution turned colourless. Ample oxygen was supplied by an aerator source, aquarium pump model NS 7200. The percentage of decolorization of the RR4 dye was determined using a HACH DR 1900 spectrometer at a wavelength of 517 nm. The dye remaining after degradation was calculated using Equation 1.

$$\text{Dye remaining (\%)} = \frac{C}{C_O} \times 100 \qquad (1)$$

From this, the efficiency of the prepared photocatalyst Pt-Bi_2WO_6/g-C_3N_4 was determined using the Langmuir Hinshelwood model Pseudo 1st Order Law which explained the kinetic reaction of the heterogenous process by plotting ln (C_o/C) against irradiation time to obtain the first-order rate constant.

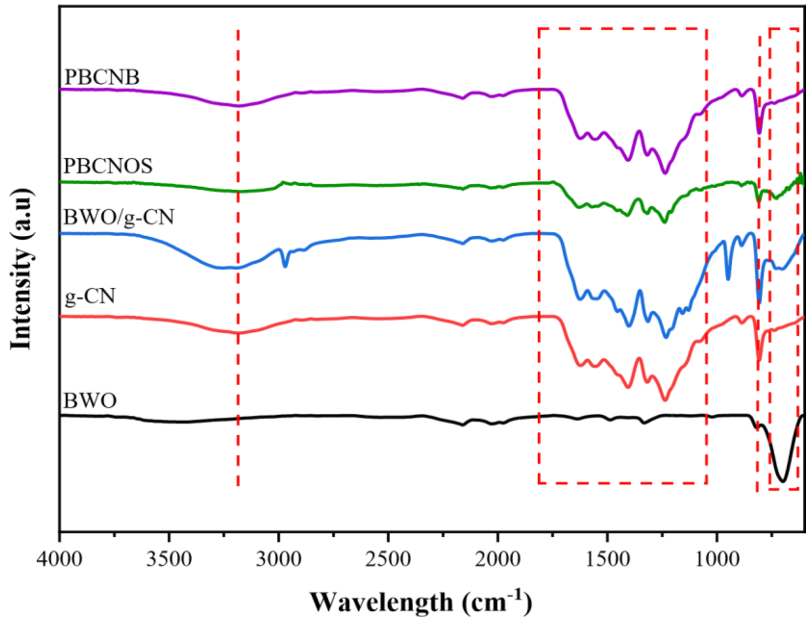

Figure 1. FTIR spectra of BWO, g-CN, BWO-g-CN, PBCN (OS) and PBCN (B).

RESULTS AND DISCUSSION

Functional Group Analysis

The FTIR spectra of the synthesized samples are displayed in Figure 1. The intense sharp peak at around 810 cm^{-1} is attributed to the breathing mode of s-triazine units of CN [19]. The absorption bands in the region of 1200–1640 cm^{-1} are attributed to the aromatic C−N stretching vibration mode [20]. The broad band centred at ~3150 cm^{-1} is attributed to the stretching mode of the N−H bond. Pure BWO exhibited major absorption bands at 500–800 cm^{-1}, which were assigned to Bi−O, W−O stretching and W–O–W bridging stretching modes [21]. All characteristic absorption bands of BWO also appeared in the spectra of BWO/CN and PBCN (OS). However, the stretching mode of the N−H bond only appeared in the spectra of g-CN and BWO/g-CN. The presence of platinum in PBCN (OS) & PBCN (B) offset the N−H bond in the composite.

Structural Analysis

In the X-ray diffractograms obtained (Figure 2), the pure g-C_3N_4 sample exhibited two prominent peaks at 10.6° and 27.5°, consistent with the (100) and (002) planes of g-C_3N_4. Pure Bi_2WO_6, exhibited a set of sharp and thin diffraction peaks that closely match its orthorhombic phase. The diffraction peaks at 2θ = 28.8°, 33.3°, 47.4°, 56.4°, 59.1°, 69.3° may be matched to the russellite phase (JCPDF: 39–0256) [22,23]. All the characteristic peaks of Bi_2WO_6 were also present in the spectra of Bi_2WO_6/g-C_3N_4 and all modified samples had (131), (200), (202), (133), (262), and (391) diffraction peaks located in similar positions. However, the peaks of g-C_3N_4 were unable to be distinguished in Bi_2WO_6/g-C_3N_4 as the characteristic diffraction peak for g-C_3N_4 at 27.2° overlaps with a prominent peak of Bi_2WO_6 at 28.6°.

Debye-Scherrer Equation:

$$D = k\lambda/\beta \text{ Cos } \theta \tag{2}$$

k = Shape factor/Sherrer equation (0.89)

β = Full width at half maximum of peak (FWHM)

λ = X-ray wavelength of K radiation

θ = Diffraction angle (radian)

Table 1. Crystallite size of synthesized materials calculated from the Debye-Scherrer Equation.

Materials	Avg. Crystallite size, D (nm)
BWO	12.09
g-CN	12.40
PBCN (B)	13.42
PBCN (OS)	20.00

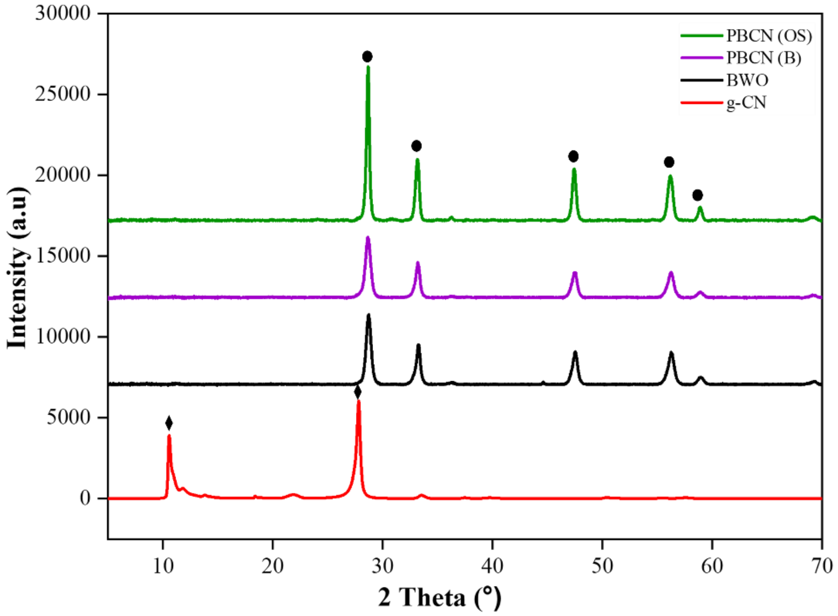

Figure 2. XRD spectra of unmodified BWO and g-CN and unmodified photocatalysts.

The crystallite sizes of the photocatalysts obtained were determined using the Debye Scherrer equation (Equation 2). It is noteworthy that a thinner peak indicates a larger crystallite size. Based on the calculation, the crystallite size of PBCN (OS) was the largest at 20 nm, whereas the others were <14 nm, as shown in Table 1. These results demonstrate the advantages of the one-step preparation method, as a larger crystallite size is preferable for this novel technology. The larger size may cause a band gap reduction due to the size quantization effect, as the larger surface-active site area may lead to better photocatalytic activity.

Morphology Analysis

FESEM-Mapping Analysis

The morphologies and structures of the samples were characterized by field emission scanning electron microscopy (FESEM). This instrument was equipped with energy dispersive X-ray spectroscopy (EDX) to determine the elemental composition of the prepared photocatalyst. As depicted in Figure 2, each sample showed a different morphology and structure, influenced by its elemental composition. For instance, a high level of bismuth in Bi_2WO_6 in Figure 3 (a) was devoted to its nanosheet structure. In addition, the fabrication of Pt-Bi_2WO_6/gC_3N_4 by two distinctive methods (batchwise and one-step preparations) led to very different morphological structures: PBCN (B) in Figure 2 (b) featured a flaky structure, while PBCN (OS) in Figure 2 (c) had a laminar structure. The high amount of bismuth, at 54.8 magnitude, and the low amount of nitrogen in PBCN (B) gave a flaky structure, whereas the 2:1 ratio of N to Bi resulted in the laminar structure of PBCN (OS). Pink dots scattered on the mapping analysis indicates the deposition of Pt scattered through the composites, while elemental composition analysis revealed a noticeable amount of Pt, at 2.3 and 3.1 for PBCN (B) and PBCN (OS), respectively.

HRTEM-SAED Analysis

To examine the morphology and crystallinity of the modified sample under PBCN (OS) to a greater extent, HRTEM studies were performed, as shown in Figure 3 (g). Pt, Bi_2WO_6 and g-C_3N_4 were found near each other after zooming in at 1000 kV. The darker sphere-shaped regions may be ascribed to Pt, whereas the lighter regions corresponded to Bi_2WO_6 regions. g-C_3N_4 [200] with lattice fringes of 0.356 nm was found located over the heterojunction interface in between two nanocomposites. A Bi_2WO_6 [131] crystal plane was observed near the lattice fringe of Pt [200] [17]. The strategic location of Pt in between two nanocomposites (Bi_2WO_6/g-C_3N_4) shows the effectiveness of the one-step approach to strategically position the Pt to act as an effective electron mediator. In addition, SAED analysis was performed to get detailed information about the diffraction area. From the images, a clear diffraction line with a square lattice pattern was observed, indicating a crystalline phase with a cubic or tetragonal symmetry which likely corresponds to Pt [200] and Bi_2WO_6 [131]. Pt [200] in the Pt^0 state was found within the orthorhombic phase of the Bi_2WO_6 matrix covered with a ring pattern that resembled the g-C_3N_4 phase. The integration of Pt within the matrix of nanocomposites showed that the one-step approach had successfully introduced Pt in between two nanocomposites and helped to boost photocatalytic activity by the formation of a Z-scheme heterojunction system [17].

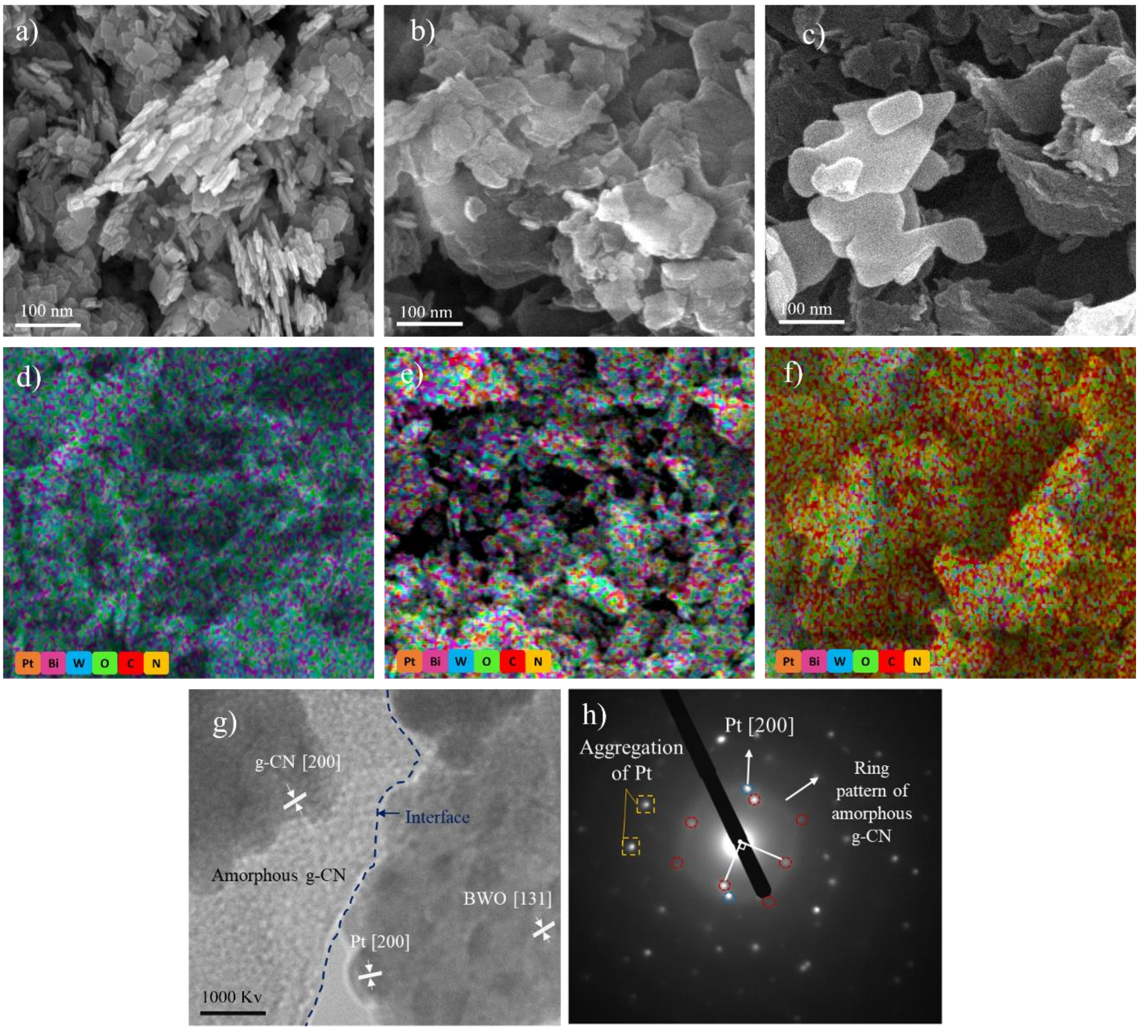

Figure 3. FESEM morphological analysis: (a) BWO, (b) PBCN (B), (c) PBCN (OS) and mapping analysis: (d) BWO, (e) PBCN (B), (f) PBCN (OS), (g) HRTEM images of PBCN (OS), (h) SAED mapping of PBCN (OS).

Optical Properties

UV-VIS Diffuse Reflectance Spectroscopy (UV VIS DRS)

The band structures of the samples were determined by the UV–VIS DRS technique. As shown in Figure 4 (a), pristine Bi_2WO_6 had an absorption edge of approximately 443 nm, which corresponded to a band gap of approximately 2.79 eV. The absorption edge of pure g-C_3N_4 was at about 457 nm, corresponding to a band gap of 2.8 eV, as ascribed in the literature. Combining these two semiconductors resulted in a gradual red shift appearing as the amount of g-C_3N_4 increased; this indicated a heterojunction formation between g-C_3N_4 and Bi_2WO_6 [14]. The band gap values were also depicted in the Tauc plot, as shown in Figure 4 (b). It is noteworthy to mention that the Bi_2WO_6/gC_3N_4 composite exhibited a smaller band gap (2.79eV) compared to pure g-C_3N_4 and Bi_2WO_6. Further, incorporating platinum into the heterojunction resulted in even lower band gaps of 2.73 eV and 2.75 eV for PBCN (B) and PBCN (OS), respectively. The visible light absorption of the Pt-Bi_2WO_6/g-C_3N_4 composites had significantly improved compared to the Bi_2WO_6/gC_3N_4 composite without platinum loading. The absorption edge was seen at a wavelength greater than 480 nm due to the surface plasmonic resonance (SPR) effect of Pt, confirming the presence of metallic Pt [17]. The findings suggest that incorporating Pt in the Bi_2WO_6/g-C_3N_4 heterojunction composite photocatalyst significantly improved its visible light absorption, thus leading to improved photocatalytic performance.

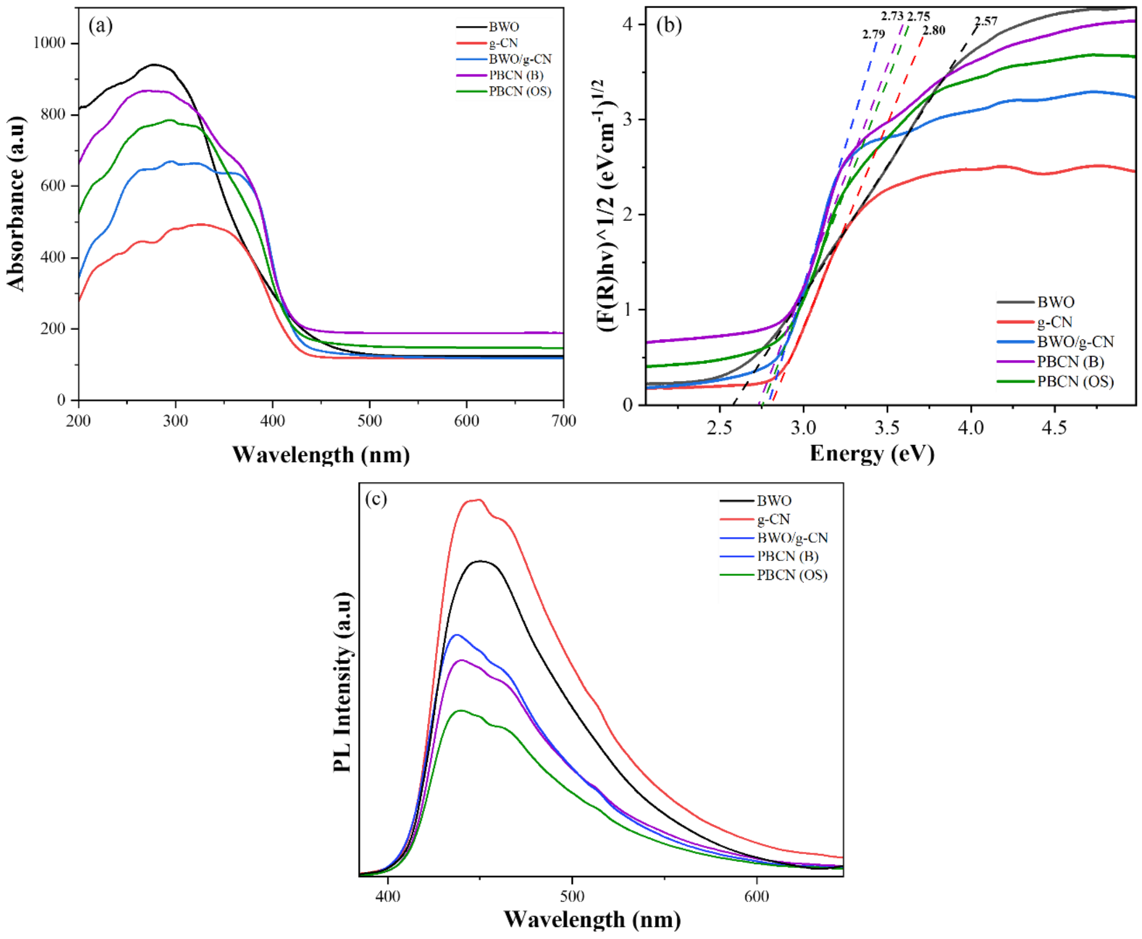

Figure 4. UV-VIS/DRS analysis of BWO, g-CN_4, BWO/g-CN, PBCN (B) and PBCN (OS): (a) Absorption spectra, (b) Tauc Plots for bandgap analysis, and (c) Photoluminescence spectra.

Photoluminescence Analysis

Photoluminescence (PL) emission spectroscopy is commonly utilized to evaluate the recombination of photoexcited carriers. In general, a lower PL intensity indicates low charge carrier recombination, resulting in high photocatalytic performance. According to Figure 4 (c), Bi_2WO_6/g-C_3N_4 had the lowest PL intensity. This was due to the heterojunction effect that significantly reduced the recombination rate of the photoexcited e/h$^+$. The introduction of platinum into the Bi_2WO_6/g-C_3N_4 composite resulted in a slightly increased PL intensity, which may be attributed to the augmented recombination rate between photoexcited electrons in CB of BWO and photogenerated holes in VB of CN on the hybrid interface. Pt^0 deposition on the surface of the CN/BWO composite functioned as a charge transmission bridge of the hybrids, denoting rich electrons in the CB of CN and holes in the VB of BWO further reducing the dissolved O_2 and the oxidation of RR4 dyes [24]. Thus, enhancing the charge separation of the Pt- Bi_2WO_6/g-C_3N_4 hybrids led to an improvement in the photocatalytic activity of the hybrid photocatalysts.

Photoelectrochemical Analysis

Photoelectrochemical tests may be used to measure the photocatalytic activity of potential photoelectrodes. Electronic impedance spectroscopy, EIS was employed to determine the mobility and recombination rate of the interface carriers, as depicted in Figure 5a (i), (ii), and (iii). All graphs resembled semicircular arcs that represent the charge transfer resistance and double-layer capacitance at the electrode-electrolyte interface in light and dark modes to observe their response toward light. A smaller semicircle radius indicates low charge transfer resistance (Rct), and thus, a better recombination rate [25]. Based on these results, pure Bi_2WO_6 had the largest impedance arc, and possessed the highest interface resistance to charge transfer. The coupling of g-C_3N_4 with Pt loading resulted in a lower charge transfer resistance which implies better charge transfer properties and potentially lower recombination rates. PBCN (OS) exhibited a slightly higher impedance radius compared to PBCN (B), indicating the higher charge transfer efficiency from the improvement of the internal charge transfer within the system, which also proves the Z-scheme heterojunction effect.

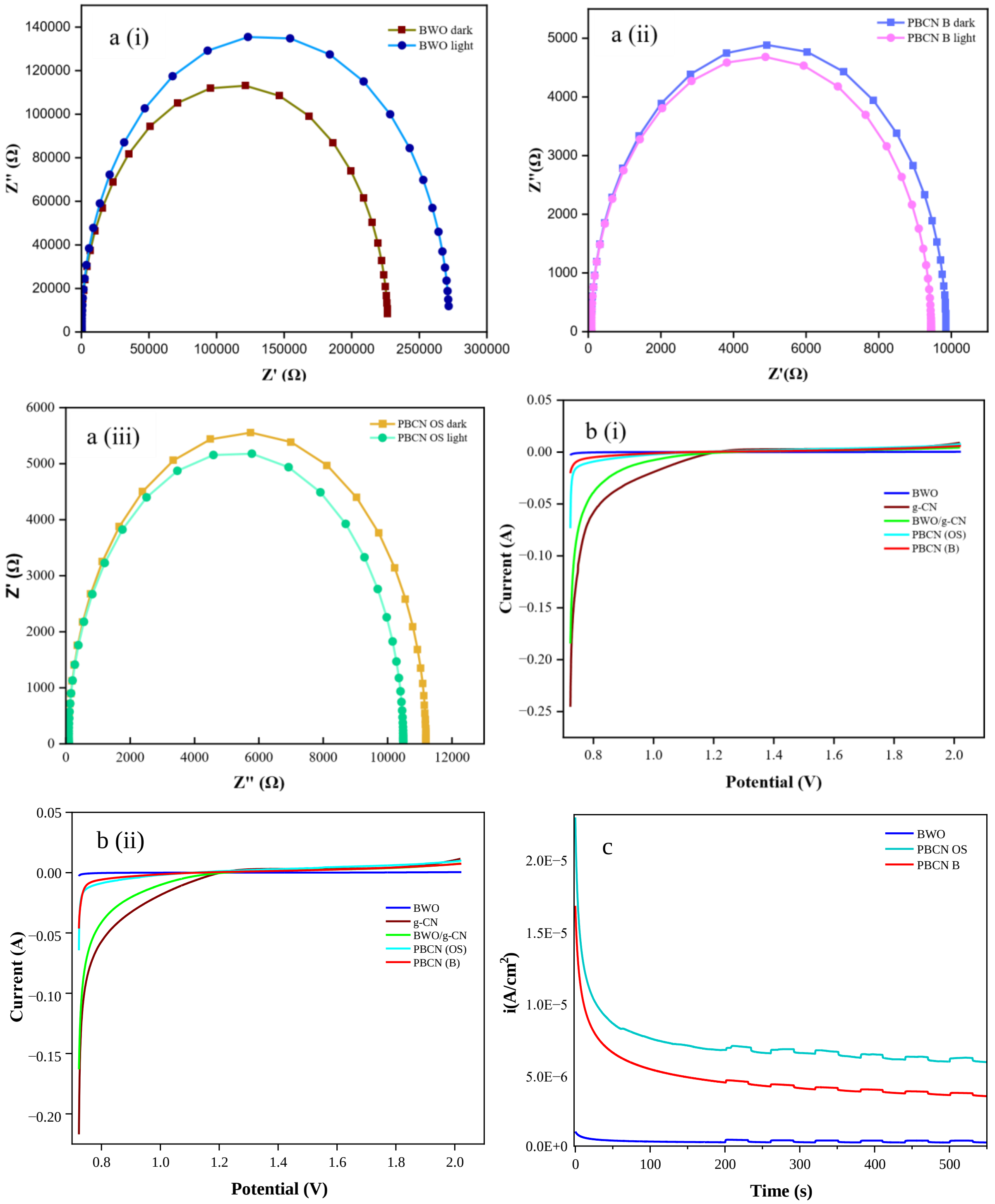

Figure 5. (a) Electrochemical impedance spectrophotometry (EIS) results: a (i) BWO, a (ii) PBCN (OS), a (iii) PBCN (B); (b) Linear Sweep Voltammetry (LSV) results: b (i) light and b (ii) dark conditions; (c) Chronoamperometry analysis results.

Linear Sweep Voltammetry (LSV)

Linear sweep voltammetry is an electrochemical method employed to deliver a progressively increasing voltage to electrodes, while simultaneously recording the generated current or current density. Concisely, an LSV plot measures the photoresponse & photooxidation of the photocatalyst under dark and light conditions [26]. Figure 5b (i) and (ii) showed that Bi_2WO_6/g-C_3N_4 exhibited increasing performance under both conditions compared to a single photocatalyst. This indicates that a good synergistic effect correlates with the fabrication of a Z-scheme heterojunction and the inclusion of a noble metal which results in the enhancement of the visible light response. Further, platinum as an efficient electron

Table 2. Recent reports on the preparation of a Z-scheme photocatalyst Bi_2WO_6, g-C_3N_4 decorated with an electron mediator, by different fabrication techniques.

Photocatalyst	Fabrication Technique	Model Pollutant	Photocatalytic Performance	Ref.
Au/g-C_3N_4/BiOBr	Hydrothermal/in-situ reduction method	Phenol	3 times higher than unmodified g-C_3N_4	[27]
Ag/g-C_3N_4/Bi_2WO_6	Hydrothermal/Photodeposition (Batchwise)	RhB Dye	1.0 wt% Ag-CN/BW > unmodified	[28]
g-C_3N_4/Au/ /Bi_2WO_6	Hydrothermal/Photodeposition (Batchwise)	RhB Dye	1.48 times and 1.62 times higher than Bi_2WO_6 and g-C_3N_4	[14]
3D/2D Bi_2WO_6/ g-C_3N_4	One-step (hydrothermal)	Atrazine	99.96% removal of ATZ	[29]
PtO_2-Pt/B Bi_2WO_6	Hydrothermal/Photodeposition (Batchwise)	CO_2 reduction	1.9 times that of pristine Bi_2WO_6	[30]
Bi_2WO_6 /QDs/ g-C_3N_4	Facile One-step (hydrothermal)	Water splitting	50 and 25 mmol/h within 4 h	[31]
Ag/AgI/Bi_2MoO_6	One-step (hydrothermal)	RhB Dye	> 98.67% degradation efficiency	[32]
F-TiO_2/g-C_3N_4	One-step	TBBPA & Sulfamethazine	> 95% degradation of TBBPA and > 98% of SMZ	[33]

mediator significantly improves photocurrent, which can be seen by the photocurrent responses of both PBCN (OS) and PBCN (B) surpassing that of Bi_2WO_6/g-C_3N_4 in either the presence or absence of light, and in which PBCN (B) offered outstanding performance.

Chronoamperometry Analysis

Chronoamperometry is an analytical method used in electrochemistry where the electrical potential of the w electrode is observed over time [34]. Based on the observations in Figure 5(c), the current of the single photocatalyst Bi_2WO_6 initially spiked before undergoing a rapid decline in the first 200 seconds before it stabilized over time. The current of PBCN (B) exhibited a smooth decay without notable fluctuations, pointing towards a more stable electrochemical environment. In contrast, for Bi_2WO_6, the current first spiked and then rapidly decayed, indicating a high initial electrochemical reaction rate. The current gradually approached a steady-state value, indicating that the electrochemical processes reached a stable equilibrium. PBCN (OS) demonstrated a slight variation in current over time, implying some evolving alterations in the electrochemical surroundings, albeit not as prominent as in Bi_2WO_6. The current steadily converged towards a more consistent level, signifying the stabilization of electrochemical reactions.

Photocatalytic Degradation Study

The overall photocatalytic performance of the samples was determined based on their degradation of Reactive Red 4-dye (RR4) under visible light irradiation, as presented in Table 3. Among all the samples tested in this study, the sample modified by one-step fabrication, PBCN (OS), exhibited excellent photocatalytic activity compared to unmodified BWO and g-CN. It nearly achieved total degradation of RR4 within 60 min and had over 85 % photocatalytic activity, followed by the sample fabricated batchwise, PBCN (B), that approached 80 % photocatalytic performance, as shown in Figure 6 (a). This indicates that the heterojunction modification of the composite with platinum generally boosted photocatalytic activity. Pt loading effectively improved charge separation efficiency resulting in stronger visible light absorption on the photocatalyst interface, as discussed in relation to Figure 3. Under the same conditions, the degradation percentage of the single photocatalysts g-CN and BWO were recorded at 51 % and 58 %, respectively. Based on this result, it can be justified that the heterojunction system offered significant photodegradation performance and photocatalytic activity. The overall performance of all synthesized photocatalysts may also be observed based on their reaction rate constants (k-value) which were calculated based on the pseudo-first-order kinetic reaction as shown in Figure 6 (b) [35].

Based on the results, the k-value increased when BWO was combined with g-CN, which is likely due to the improvement in the charge separation from the heterojunction effect. In contrast, the modified photocatalyst PBCN (OS), gave the highest photocatalytic activity and outstanding efficiency with its k-value at 0.025 min^{-1}. This proves that the introduction of Pt using a one-step technique was the best approach to provide the optimum conditions for it to play its role as an electron shuttle mediator and improve the Z-scheme heterojunction system.

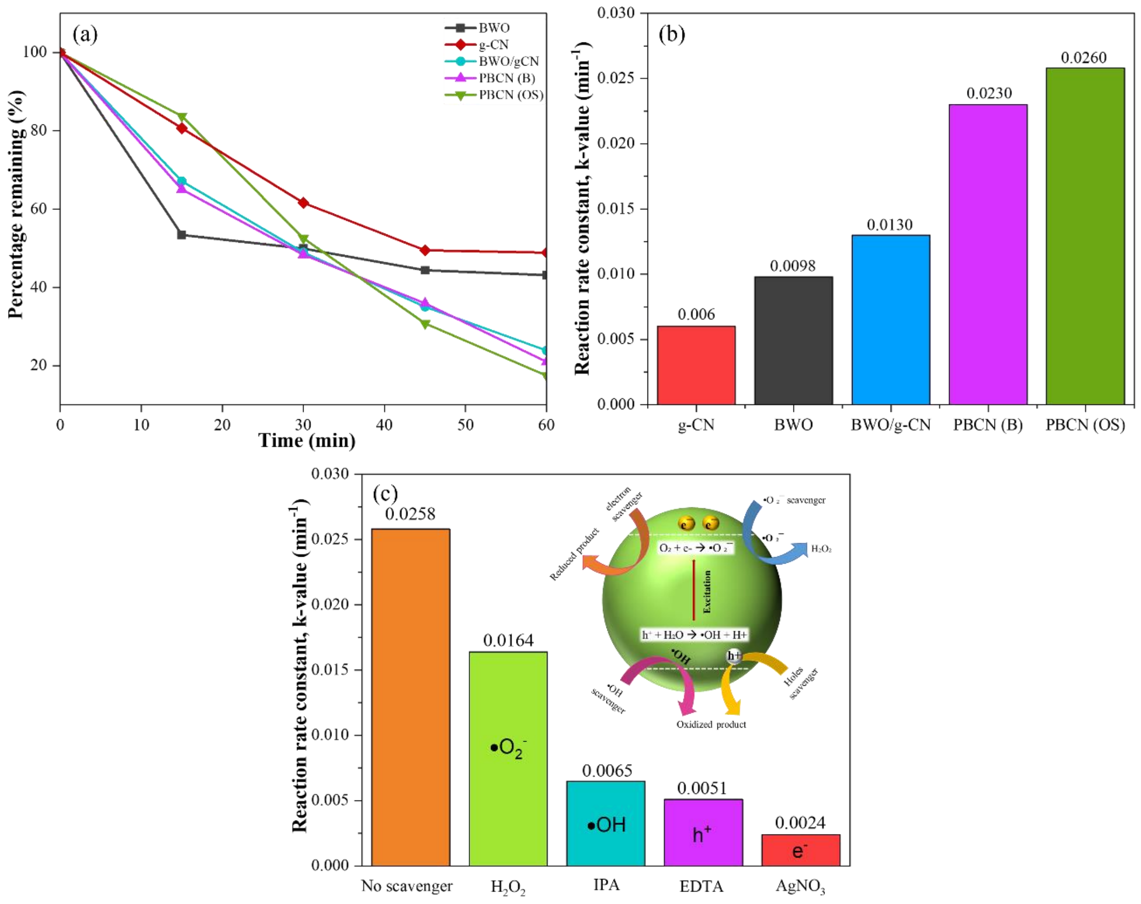

Figure 6. (a) Percentage of RR4 dye remaining over time with all synthesized materials, (b) Reaction rate constant (min^{-1}) of synthesized materials based on pseudo-first-order kinetics, (c) Radical trapping test analysis of PBCN (OS).

Table 3. Photocatalytic performance based on percentage remaining from dye degradation and reaction rate constant (k-value) based from pseudo-first-order kinetics.

Material	**Percentage remaining (%)**	**Reaction rate constant, k (min^{-1})**
BWO	42	0.0142
g-CN	49	0.006
BWO/g-CN	23	0.0129
PBCN (B)	24	0.0052
PBCN (OS)	18	0.0155

Radical Trapping Test and Proposed Z-scheme Mechanism

A radical trapping test was conducted to evaluate the reactive radical species involved in the photodegradation of RR4 dyes under simulated light, and an optimum sample of PBCN (OS) was used in the process. Four major species were observed in photocatalysis in the presence of a scavenger to quench each specific radical: the superoxide anion, hydroxyl ion, holes and electrons. Figure 6(c) shows the photocatalytic efficiency after the addition of scavengers for different species. Based on these results, addition of H_2O_2 into the degradation system caused the least reduction in photocatalytic performance, showing that $•O_2^-$ played a minor role in the degradation of RR4 dye, which implies that oxygen reduction may not be prominent in the system. The addition of IPA led to a significant drop in photocatalytic performance, suggesting that •OH was one of the key contributors in the degradation, especially in breaking down organic pollutants such as RR4. The decrease in the k-value after introducing the hole scavenger (EDTA) indicates that h+ also played a crucial role. This proved the presence of a Z-scheme heterojunction route within the system based on the effectiveness of Pt as an electron mediator during the degradation process. The abundance of h^+ played a major role in either directly oxidizing the RR4 dye (due to the high oxidation potential of holes in the valence band of Bi_2WO_6) or in generating another reactive species such as •OH. Remarkably, the addition of $AgNO_3$ gave the lowest photocatalytic performance, indicating that e- was the most dominant species during the photocatalytic process.

A good Z-scheme facilitation mechanism makes weak electrons in the CB of Bi_2WO_6 move toward weak h^+ in the VB of g-C_3N_4 leaving the strong e^- at the top of the VB of g-C_3N_4, promoting the formation of more active species and increasing the overall photocatalytic performance in degrading RR4 dye as in Figure 7 [36]. This shows that the optimum position of Pt as an electron mediator likely enhanced the charge separation between Bi_2WO_6 and g-C_3N_4, allowing more electrons and holes to participate in the degradation process.

CONCLUSION

Pt- Bi_2WO_6/g-C_3N_4 was successfully fabricated using both batchwise and one-step preparation methods. The introduction of Pt as an electron mediator using a one-step fabrication technique exhibited the best photocatalytic properties, as discussed in a series of characterizations, and had the highest photocatalytic activity, with a k-value of 0.0258 min^{-1}. This showed that the incorporation of Pt into the BWO/g-CN composite with the one-step approach, in which Pt was placed in the middle of two nanocomposites, had a significant impact on the recombination rate of the charge carrier, and consequently overcame the limitations of a single photocatalyst.

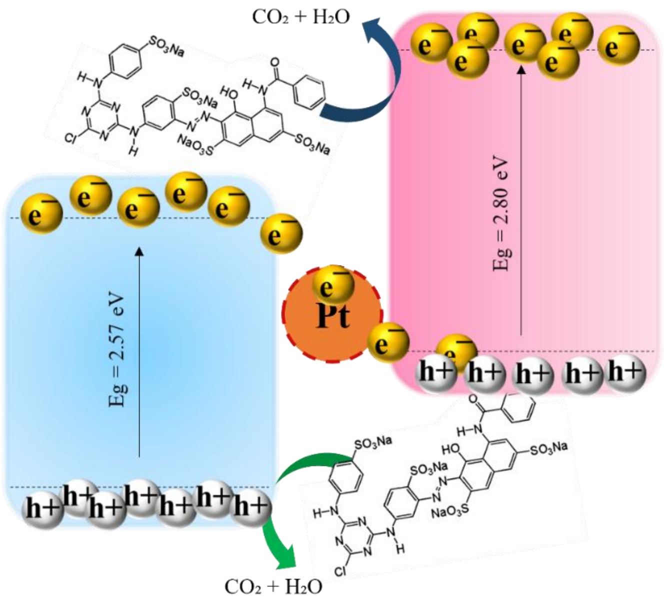

Figure 7. Schematic illustration of the Z-scheme mechanism in Pt-Bi_2WO_6/g-C_3N_4.

ACKNOWLEDGEMENT

We would like to acknowledge Universiti Teknologi MARA (UiTM) for providing all the facilities for the completion of this research. This work was also supported by the Ministry of Higher Education (MOHE) under the Fundamental Research Grant Scheme: FRGS/1/2022/STG04/UiTM/02/1.

REFERENCES

1. Azanaw, A., Birlie, B., Teshome, B. & Jemberie, M. (2022) Textile effluent treatment methods and eco-friendly resolution of textile wastewater. *Case Studies in Chemical and Environmental Engineering*, **6**, 100230, (2022b).

2. Kishor, R., Purchase, D. & Dattatraya, G. (2021). Environment-friendly degradation and detoxification of Congo red dye and textile industry wastewater by a newly isolated *Bacillus cohnni (RKS9). Environmental Technology & Innovation*, **22**.

3. Parasuraman, B., Shanmugam, P. & Govindasamy, P. (2023) Photocatalytic degradation of tetracycline contaminated wastewater over Bi_2S_3/$BiWO_6$ rGO ternary nanocomposite under visible light irradiation. *Journal of the Taiwan Institute of Chemical Engineers,* **166**, 105249.

4. Li-Ming, Z., Lu-E, S., Zhi-Liang, Z., Jian-Min, C., Dong-Dong, S. & Zhen-Xing, T. (2011) Preparation and application of chitosan nanoparticles and nanofibers. Brazilian Journal of Chemical Engineering, **28(3)**, 1–15.

5. Ketwong, P., Takashima, M., Nitta, A., Pookmanee, P. & Ohtani, B. (2018) Hydrothermal synthesis and photocatalytic activities of stabilized bismuth vanadate/bismuth tungstate composites. *Journal of Environmental Chemical Engineering*, **6(2)**, 2048–2054

6. Khan, M. M., Adil, S. F. & Al-Mayouf, A. (2015) Metal oxides as photocatalysts. *Journal of Saudi Chemical Society*, **19(5)**, 462–464.

7. Quan, W., Bao, J., Meng, X., Ning, Y., Cui, Y., Hu, X., Yu, S. & Tian, H. (2023) 2D/2D Z-scheme photocatalyst of g-C_3N_4 and plasmonic bi metal deposited Bi_2WO_6: Enhanced separation and migration of photoinduced charges. *Journal of Alloys and Compounds*, **946**, 169396.

8. Hoang, L. H., Phu, N. D., Peng, H. & Chen, X. (2018) High photocatalytic activity N- doped Bi_2WO_6 nanoparticles using a two-step microwave-assisted and hydrothermal synthesis. *Journal of Alloys and Compounds*, **744**, 228–233.

9. Mandyal, P., Guleria, A., Sharma, R., Sambyal, S., Priye, A., Fang, B. & Shandilya, P. (2022) Insight into the properties, morphologies and photocatalytic applications of Scheme Bi_2WO_6. *Journal of Environmental Chemical Engineering*, **10(6)**, 108918.

10. Li, K., Teng, C., Wang, S. & Min, Q. (2021) Recent Advances in TIO_2-Based heterojunctions for photocatalytic CO_2 reduction with water oxidation: a review. *Frontiers in Chemistry*, **9**.

11. Afroz, K., Moniruddin, M., Bakranov, N., Kudaibergenov, S. & Nuraje, N. (2018) A heterojunction strategy to improve the visible light sensitive water splitting performance of photocatalytic materials. *Journal of Materials Chemistry A*, **6(44)**, 21696–21718.

12. Shanmugam, P., Meejoo, S. & Boonyuen, S. (2023) In-situ development of boron doped g-C_3N_4 supported SBA-15 nanocomposites for photocatalytic degradation of tetracycline. *Environmental research*, **224,** 115496.

13. Chong, B., Chen, L., Wang, W., Han, D., Wang, L., Feng, L., Li, Q. & Li, C. (2017) Visible-light-driven Ag-decorated g-C_3N_4/Bi_2WO_6 Z-scheme composite for high photocatalytic activity. *Materials Letters*, **204**, 149–153.

14. Li, Q., Lu, M., Wang, W., Zhao, W., Chen, G. & Shi, H. (2020) Fabrication of 2D/2D g-C_3N_4/Au/Bi_2WO_6 Z-scheme photocatalyst with enhanced visible-light-driven photocatalytic activity. *Applied Surface Science*, **508**, 144182.

15. Khedr, T. M., Wang, K., Kowalski, D., El-Sheikh, S. M., Abdeldayem, H. M., Ohtani, B. & Kowalska, E. (2022) Bi_2WO_6-based Z-scheme photocatalysts: Principles, mechanisms and photocatalytic applications. *Journal of Environmental Chemical Engineering*, **10(3)**, 107838.

16. Yu, H., Huang, Y., Gao, D., Wang, P. & Tang, H. (2019) Improved H_2 -generation performance of Pt/CdS photocatalyst by a dual-function TiO_2 mediator for effective electron transfer and hole blocking. *Ceramics International*, **45(8)**, 9807–9813.

17. Zhang, Y., Chai, C., Zhang, X., Liu, J., Duan, D., Fan, C. & Wang, Y. (2019) Construction of Pt-decorated g-C_3N_4/Bi_2WO_6 Z-scheme composite with superior solar photocatalytic activity toward rhodamine B degradation. *Inorganic Chemistry Communications/Inorganic Chemistry Communications (Online)*, **100**, 81–91.

18. Chen, P., Di, S., Qiu, X. & Zhu, S. (2022). One-step synthesis of F-TiO_2/g-C_3N_4 heterojunction as highly efficient visible light active catalysts for tetrabromobisphenol A and sulfamethazine degradation. *Applied Surface Science*, **587**, 152889.

19. Sunasee, S., Leong, K. H., Wong, K. T., Lee, G., Pichiah, S., Nah, I., Jeon, B., Yoon, Y. & Jang, M. (2017) Sonophotocatalytic degradation of bisphenol A and its intermediates with graphitic carbon nitride. *Environmental Science and Pollution Research International*, **26(2)**, 1082–1093.

20. Pareek, S., Sharma, M., Lal, S. & Quamara, J. K. (2018) Polymeric graphitic carbon nitride–barium

titanate nanocomposites with different content ratios: a comparative investigation on dielectric and optical properties. *Journal of Materials Science. Materials in Electronics*, **29(15)**, 13043–13051.

21. Zhou, K., Lu, J., Yan, Y., Zhang, C., Qiu, Y. & Li, W. (2020) Highly efficient photocatalytic performance of BiI/Bi2WO6 for degradation of tetracycline hydrochloride in an aqueous phase. *RSC Advances*, **10(20)**, 12068–12077.

22. Truong, H. B., Huy, B., Ray, S. K., Lee, Y., Cho, J. & Hur, J. (2021) Visible light-activated NGQD/ nsC_3N_4/Bi_2WO_6 microsphere composite for effluent organic matter treatment. *Chemical Engineering Journal*, **415**, 129024.

23. Guan, Z., Li, X., Wu, Y., Chen, Z., Huang, X., Wang, D., Yang, Q., Liu, J., Tian, S., Chen, X. & Zhao, H. (2021). AgBr nanoparticles decorated 2D/2D GO/Bi_2WO_6 photocatalyst with enhanced photocatalytic performance for the removal of tetracycline hydrochloride. *Chemical Engineering Journal*, **410**, 128283.

24. Katsumata, H., Sakai, T., Suzuki, T. & Kaneco, S. (2014) Highly Efficient Photocatalytic Activity of g-C_3N_4/Ag_3PO_4 Hybrid Photocatalysts through Z-Scheme Photocatalytic Mechanism under Visible Light. *Industrial & Engineering Chemistry Research*, **53(19)**, 8018–8025.

25. Lin, C., Zhuang, Y., Tsai, D., Wei, H. & Liu, T. (2020) Performance Enhancement of Vanadium Redox Flow Battery by Treated Carbon Felt Electrodes of Polyacrylonitrile using Atmospheric Pressure Plasma. *Polymers*, **12(6)**, 1372.

26. Abass, N. A., Qahtan, T., Gondal, M., Moqbel, R. & Bubshait, A. (2020) Laser-assisted synthesis of ZnO/ZnSe hybrid nanostructured films for enhanced solar-light induced water splitting and water decontamination. *International Journal of Hydrogen Energy*, **45(43)**, 22938–22949.

27. Wang, L., Zhang, H. G., Guo, C. Y., Feng, L. J., Li, C. H. & Wang, W. T. (2019) Facile constructing plasmonic Z-scheme Au NPs/ g-C_3N_4/BiOBr for enhanced visible light photocatalytic activity. *Ranliao Huaxue Xuebao/ Journal of Fuel Chemistry and Technology*, **47(7)**, 834–842.

28. Chong, B., Chen, L., Wang, W., Han, D., Wang, L., Feng, L., Li, Q. & Li, C. (2017) Visible-light-driven Ag-decorated g-C_3N_4/Bi_2WO_6 Z-scheme composite for high photocatalytic activity. *Materials Letters*, **204**, 149–153.

29. Yang, C., Chai, H., Xu, P., Wang, P., Wang, X., Shen, T., Zheng, Q. & Zhang, G. (2022) One-step synthesis of a 3D/2D Bi_2WO_6/g-C_3N_4 heterojunction for effective photocatalytic degradation of atrazine: Kinetics, degradation mechanisms and ecotoxicity. *Separation and Purification Technology*, **288**, 120609.

30. Jiang, H., An, Q., & Zang, S. (2023). *Journal of Environmental Chemical Engineering* Toward efficient photocatalytic CO_2 reduction under visible light irradiation. **11** (May).

31. Hao, H., Lu, D. & Wang, Q. (2018) Photo-electrochemical study on charge separation mechanisms of Bi_2WO_6 quantum dots decorated g-C3N4. *International Journal of Hydrogen Energy*, **43(18)**, 8824–8834.

32. Phuruangrat, A., Suriyarpitak, K., Wannapop, S., Thongtem, T. & Thongtem, S. (2023) Synthesis of Z-scheme Ag/AgI/Bi2 MoO_6 nanocomposites used for high-efficiency visible-light-driven photocatalyst. *Desalination and Water Treatment*, **308**, 150–159.

33. Chen, P., Di, S., Qiu, X. & Zhu, S. (2022) One-step synthesis of F-TiO_2/g-C_3N_4 heterojunction as highly efficient visible-light-active catalysts for tetrabromobisphenol A and sulfamethazine degradation. *Applied Surface Science*, **587**, 152889.

34. Baluta, S., Meloni, F., Halicka, K., Szyszka, A., Zucca, A., Pilo, M. I. & Cabaj, J. (2022) Differential pulse voltammetry and chronoamperometry as analytical tools for epinephrine detection using a tyrosinase-based electrochemical biosensor. *RSC Advances*, **12(39)**, 25342–25353.

35. Adzis, N. S., Suhaimi, N. H. S., Abdul Ghani, N. I., Abd Yami, N. F. N., Muhamad, N. A., Mohd Azami, M. S., & Nawawi, W. I. (2023). Modification of Silver Oxide/Silver Doped Titanium Dioxide (Ag_2O/Ag-TiO_2) photocatalyst using an immobilized reverse photodeposition method for photodegradation of Reactive Red 4 dye. *Malaysian Journal of Chemistry*, **25(4)**, 184–198.

36. Suhaimi, N. H. S., Azhar, R., Adzis, N. S., Mohd Ishak, M. A., Ramli, M. Z., Hamzah, M. Y., Ismail, K., & Nawawi, W. I. (2025). Recent updates on TiO_2-based materials for various photocatalytic applications in environmental remediation & energy production. *Desalination and Water Treatment*, **321**, 100976.